H-ferritin–nanocaged doxorubicin nanoparticles specifically target and kill tumors with a single-dose injection

Minmin Liang[a,1], Kelong Fan[a,b,1], Meng Zhou[a,b], Demin Duan[a], Jiyan Zheng[a], Dongling Yang[a], Jing Feng[a], and Xiyun Yan[a,2]

[a]Key Laboratory of Protein and Peptide Pharmaceutical, National Laboratory of Biomacromolecules, Chinese Academy of Sciences–University of Tokyo Joint Laboratory of Structural Virology and Immunology, Institute of Biophysics, Chinese Academy of Sciences, Beijing 100101, China; and [b]University of Chinese Academy of Sciences, Beijing 100049, China

Edited by Jiayang Li, Chinese Academy of Sciences, Beijing, China, and approved September 4, 2014 (received for review April 29, 2014)

An ideal nanocarrier for efficient drug delivery must be able to target specific cells and carry high doses of therapeutic drugs and should also exhibit optimized physicochemical properties and biocompatibility. However, it is a tremendous challenge to engineer all of the above characteristics into a single carrier particle. Here, we show that natural H-ferritin (HFn) nanocages can carry high doses of doxorubicin (Dox) for tumor-specific targeting and killing without any targeting ligand functionalization or property modulation. Dox-loaded HFn (HFn-Dox) specifically bound and subsequently internalized into tumor cells via interaction with overexpressed transferrin receptor 1 and released Dox in the lysosomes. In vivo in the mouse, HFn-Dox exhibited more than 10-fold higher intratumoral drug concentration than free Dox and significantly inhibited tumor growth after a single-dose injection. Importantly, HFn-Dox displayed an excellent safety profile that significantly reduced healthy organ drug exposure and improved the maximum tolerated dose by fourfold compared with free Dox. Moreover, because the HFn nanocarrier has well-defined morphology and does not need any ligand modification or property modulation it can be easily produced with high purity and yield, which are requirements for drugs used in clinical trials. Thus, these unique properties make the HFn nanocage an ideal vehicle for efficient anticancer drug delivery.

An ideal nanocarrier for efficient drug delivery must be able to target specific cells and carry high doses of therapeutic drugs and should also exhibit optimized physicochemical properties and biocompatibility (1–3). However, it is a tremendous challenge to engineer all of the above characteristics into a single carrier particle (4–6). Ferritin is a spherical iron storage protein composed of 24 subunits of two types, heavy-chain ferritin (HFn) and light-chain ferritin (LFn). Ferritin protein self-assembles naturally into a hollow nanocage with an outer diameter of 12 nm and an interior cavity 8 nm in diameter (7). The cavity is a useful template for synthesizing highly crystalline and monodisperse nanoparticles (NPs) (8–10). Recently, it was reported that HFn binds to human cells via interacting with the transferrin receptor 1 (TfR1) (11). Although it is well known that TfR1 is highly expressed on human cancer cells and has long been used as a targeting marker for tumor diagnosis and therapy, current HFn-based methods for tumor detection and treatment still rely on functionalization of HFn with recognition ligands to achieve tumor-specific targeting (12–16).

By using the intrinsic tumor-targeting properties of HFn, we recently reported that iron-encapsulated HFn NPs specifically target and visualize tumor tissues without the use of additional targeting ligands or signal molecules (17). In the present study, we loaded HFn nanocage with doxorubicin (Dox) for tumor-specific drug delivery. HFn nanocages can encapsulate large amounts of foreign molecules (18–24), bind specifically to tumor cells that overexpress TfR1 (17), and should be able to efficiently deliver high doses of therapeutic drugs to tumors. In particular, natural HFn nanocarriers are expected to possess an outstanding biocompatibility and safety profile, because they exist naturally in the human body and are composed of nontoxic elements that therefore would not activate inflammatory or immunological responses (25). In addition, HFn can be produced economically in *Escherichia coli* and can be purified easily by exploiting their heat-resistant property (17, 26). The production and purification characteristics of the HFn nanocarriers are effective for scale-up of the manufacturing process with robust and reproducible procedures.

Although ferritin-based drug delivery has been recently developed for cancer treatment, in almost all published studies ferritin was modified with recognition ligands to achieve tumor-specific targeting (12–15). These extra surface modifications destroy the intrinsic tumor-specific binding of natural ferritin and disturb its in vivo performance and biocompatibility because of the altered surface physicochemical properties of ferritin. In addition, it was shown recently that the foreign ligands introduced by genetic engineering affect the self-assembling process of ferritin during their expression in *E. coli*, and thus result in a low yield of the final products (27–29) [e.g., the typical yields of RGD-modified HFn are less than 1/10 those of free HFn (26)].

In addition, many currently available methods for drug loading into ferritin involves disassembling ferritin nanocages in severe acidic pH (18–22), which irreversibly damages ferritin protein cages and forms hole defects on the spherical protein surface (30). The irreversible damages to ferritin will seriously affect their in vivo stability and drug delivery efficiency. So far, most of

Significance

Nanoparticles capable of specifically binding to target cells and delivering high doses of therapeutic drugs with optimized safety profiles are much sought after in the nanomedical field. Here, we developed a natural H-ferritin (HFn) nanocarrier that specifically delivered a high concentration of the therapeutic drug doxorubicin (Dox) to tumor cells and significantly inhibited tumor growth with a single-dose treatment while also showing excellent biocompatibility and safety profiles in murine cancer models. Compared with the clinically approved liposomal Dox (Doxil), HFn-Dox exhibited longer median survival times and lower toxicity when administered at the same dose in all tumor models studied.

Author contributions: M.L., K.F., and X.Y. designed research; M.L., K.F., M.Z., D.D., J.Z., D.Y., and J.F. performed research; M.L., K.F., and X.Y. analyzed data; and M.L. and K.F. wrote the paper.

The authors declare no conflict of interest.

This article is a PNAS Direct Submission.

[1]M.L. and K.F. contributed equally to this work.

[2]To whom correspondence should be addressed. Email: yanxy@ibp.ac.cn.

This article contains supporting information online at www.pnas.org/lookup/suppl/doi:10.1073/pnas.1407808111/-/DCSupplemental.

the published work on ferritin-based drug delivery only reported in vitro results (18–21), reflecting that the drug-loaded ferritin prepared using the acidic pH method might not be suitable for in vivo applications.

Results

Human HFn was expressed and purified from *E. coli*, as previously described (17). HFn-Dox NPs were prepared by loading Dox into the cavities of HFn nanocages through disassembling HFn in 8 M urea in the presence of Dox, followed by a reassembling process with a series of stepwise gradients of urea from 8 M to 0 M in PBS buffer (Fig. 1*A*). The loading of Dox into the HFn nanocages is dependent on their electrostatic interactions. Because the pK_a of Dox is 8.2 (31), it can easily bind to the negatively charged internal surface of ferritin (32) in the neutral loading buffer. Size-exclusion chromatography confirmed the successful loading of Dox into HFn nanocages, and the amount of encapsulated Dox was determined to be 33 Dox molecules per HFn nanocage (Fig. S1*A*). Purified HFn-Dox NPs were further analyzed by cryoelectron transmission microscopy. Both HFn and HFn-Dox were monodispersed in solution with a well-defined spherical morphology (Fig. 1*B*). Dynamic light scattering (DLS) analysis showed that the HFn-Dox NPs had a narrow size distribution, and there was no significant difference observed in size between HFn (mean = 14.1 nm) and HFn-Dox (mean = 14.2 nm) (Fig. 1*C*). The CD spectra of HFn-Dox were almost identical to that of HFn (Fig. S1*B*), indicating that Dox loading does not affect the structural conformation of the HFn nanocage, implying that it refolds into its native state upon the loading process.

The stability of HFn-Dox NPs was evaluated by incubating HFn-Dox in mouse serum at 37 °C, and monitored for Dox release by HPLC. No substantial drug release from HFn nanocages

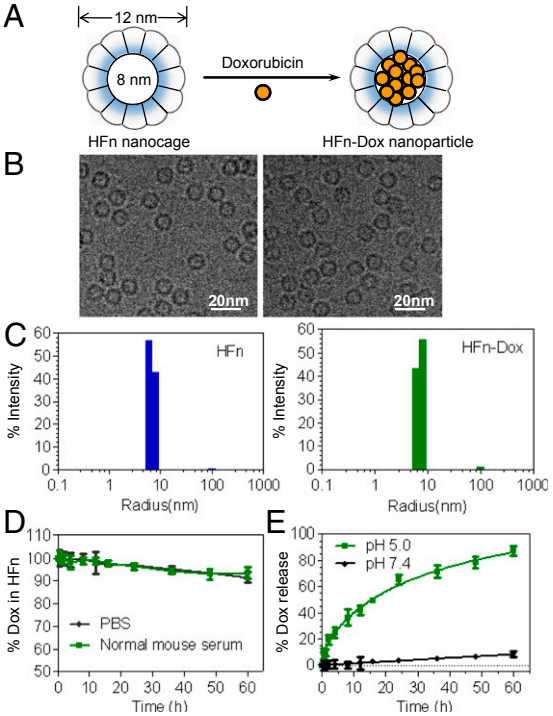

Fig. 1. Preparation and characterization of HFn-Dox NPs. (*A*) Schematic depiction of the Dox loading process. (*B*) Cryo-EM images of HFn nanocages (*Left*) and HFn-Dox NPs (*Right*). (*C*) DLS analysis of HFn nanocages and HFn-Dox NPs. (*D*) Stability of HFn-Dox NPs in mouse serum at 37 °C over 60 h of incubation (n = 3, bars represent means ± SD). (*E*) The kinetics of Dox release from HFn-Dox at pH 5.0 and pH 7.0 at 37 °C (n = 3, bars represent means ± SD).

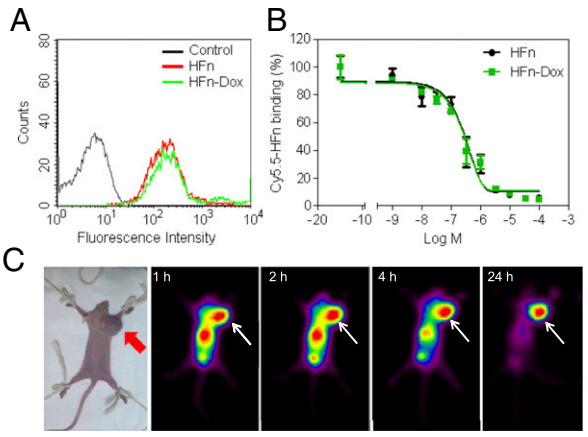

Fig. 2. HFn-Dox specifically targets tumor cells in vitro and in vivo. (*A*) Flow cytometric analysis of the specific binding of HFn and HFn-Dox to HT-29 colon cancer cells. (*B*) Inhibition of the binding of Cy5.5-labeled HFn to HT-29 cells by unlabeled HFn or HFn-Dox. The IC_{50} values of HFn and HFn-Dox were 0.25 ± 0.010 μM and 0.26 ± 0.012 μM, respectively (n = 4, bars represent means ± SD). (*C*) In vivo nuclear imaging of HT-29 tumors. Mice were injected i.v. with 400 μCi of ^{125}I-labeled HFn-Dox and imaged for 24 h. Arrows mark the tumor location.

was detected over a 60-h period of incubation (Fig. 1*D*), suggesting that HFn-Dox NPs is sufficiently stable during delivery of its drug load through the systemic circulation.

HFn nanocages disassemble into protein subunits under acidic conditions and release the encapsulated molecules (33). To verify the pH-dependent kinetics of drug release of our HFn-Dox NPs, they were incubated either at pH 7.4 or pH 5.0 at 37 °C for 60 h and the release of Dox was monitored using HPLC (Fig. 1*E*). At pH 7.4, HFn-Dox NPs were stable, and no significant release of free drug was observed over 60 h of incubation. In contrast, at pH 5.0, free Dox was detected with a drug release half-life of 14 h and reached a maximum release of 87 ± 3% at 60 h. These results suggest that a potential endo/lysosome-based drug release mechanism exists for the HFn drug delivery vehicle.

We have previously shown that HFn can specifically target tumor cells that overexpress TfR1 (17). To confirm the specific binding of HFn-Dox NPs to live tumor cells, flow cytometry and confocal analysis were performed on TfR1 overexpressed HT-29 human colon cancer cells after incubation with HFn-Dox. HFn-Dox, as expected, bound to HT-29 cells (Fig. 2*A*), and the binding was significantly inhibited by an anti-TfR1 mAb (Fig. S2), indicating a specific binding of HFn-Dox to TfR1 on HT-29 cells. We further quantitatively compared the binding activity of HFn-Dox and HFn to TfR1 using competitive binding assay. HT-29 cells were incubated with Cy5.5-labeled HFn in the presence of increasing concentrations of unlabeled HFn or HFn-Dox. Analysis of the competitive binding curves demonstrated that the IC_{50} values for HFn-Dox and HFn were 0.25 ± 0.010 μM and 0.26 ± 0.012 μM under identical experimental conditions (Fig. 2*B*), confirming that Dox loading has no effect on the tumor cell binding activity of the HFn nanocage.

To further test its in vivo tumor-targeting capability, HFn-Dox was radiolabeled with ^{125}I and injected i.v. for tumor-bearing mouse imaging. Because of the resolution limit of the clinical γ-camera (34), mice were imaged when tumor volumes were >1 cm^3. As shown in Fig. 2*C*, the HT-29 tumor was clearly visualized with a high contrast to the nonspecific organ background, which was rapidly cleared from the body within 24 h, indicating that HFn-Dox is capable of binding specifically to tumors in vivo and can be eliminated rapidly from the body if not bound to the desired tumors. These results suggest that this newly developed HFn nancarrier should be able to deliver the

encapsulated Dox to tumors in vivo while being efficiently cleared from healthy organs, thus avoiding systemic adverse reactions.

To explore the underlying mechanisms of HFn-Dox internalization and intracellular drug release, we labeled HFn-Dox with Cy5.5 on the surface of HFn nanocages and incubated them with HT-29 tumor cells for fluorescence microscopy observation. Cells were stained with the lysosomal marker Lamp1 to observe the potential lysosome-based drug release process. As shown in Fig. 3, HFn-Dox rapidly bound to the surface of HT-29 cells once incubated with the cells. At 24 h postincubation, HFn-Dox was located in both the cytoplasm and lysosomes, as shown by its colocalization with Lamp1 (Fig. 3 *B*, *F*, *J*, and *N*). At 48 h postincubation, the majority of HFn-Dox was found in lysosomes (Fig. 3 *C*, *G*, and *K*), where Dox was gradually released from HFn nanocages and subsequently translocated into the nucleus (Fig. 3*O*). At 72 h, cell nuclei were intensely stained with Dox, and cells were found to be in the process of apoptosis (Fig. 3 *I* and *P*). After release of the encapsulated Dox, HFn nanocages were finally biodegraded into free amino acids within the lysosomes, as evident from the decline of Cy5.5 fluorescence (Fig. 3*D*), which marked the surface of HFn. These data demonstrate that the specific binding of HFn-Dox to HT-29 tumor cells leads to the endocytosis of HFn-Dox with subsequent trafficking of HFn-Dox into lysosomes, followed by the intracellular drug release and tumor cell apoptosis.

To study the pharmacokinetic behavior of HFn-Dox NPs, healthy BALB/c mice were administered HFn-Dox i.v.; the plasma samples at different time points over the course of 25 h were collected and the Dox concentration was measured by its fluorescence (Fig. 4*A*). The measured blood elimination half-life and area under the concentration time curve (AUC) of HFn-Dox were 256 ± 19.0 min and 1,192 ± 99.38%ID·mL^{-1}·min^{-1} (percentage of injected dose per milliliter per minute) . In contrast, the blood half-life and AUC of free Dox at the same dose were only 21 ± 6.4 min and 5.7 ± 0.33%ID·mL^{-1}·min^{-1}. The significantly longer plasma half-life and higher AUC of HFn-Dox are likely to improve drug retention in the systemic circulation and facilitate time-dependent drug accumulation in tumors.

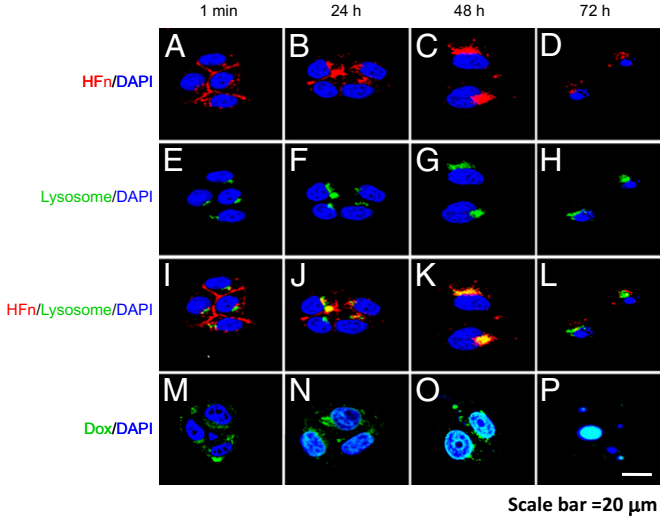

Fig. 3. Confocal images of the intracellular uptake of HFn-Dox and delivery of Dox to the nucleus in HT-29 tumor cells. HT-29 cells were incubated at 37 °C with Cy5.5-labeled HFn-Dox for the times indicated, followed by staining with the lysosomal marker Lamp1 to show the process of HFn-Dox cellular trafficking (*A*–*L*). HT-29 cells were incubated with HFn-Dox to show the trafficking of Dox to the nucleus (*M*–*P*). (Scale bar, 20 μm.)

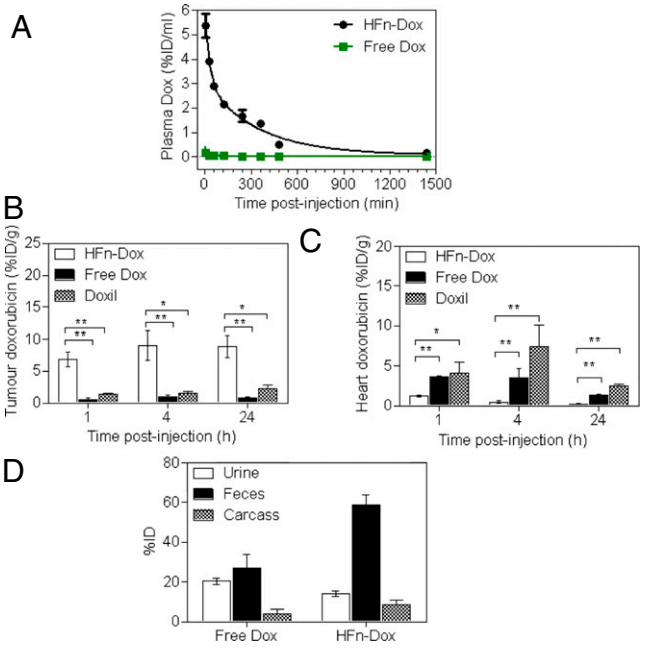

Fig. 4. Plasma pharmacokinetics, tissue biodistribution, and total body clearance of HFn-Dox NPs. (*A*) Plasma concentrations of Dox as a function of postinjection time. (*B* and *C*) The concentrations of Dox in tumor (*B*) and heart tissue (*C*) at 1, 4, and 24 h postinjection ($n = 4$, bars represent means ± SD, Student t test, $^*P < 0.01$, $^{**}P < 0.001$ versus HFn-Dox–treated mice). (*D*) Elimination of HFn-Dox and free Dox in excrement and retained doses in carcass of healthy mice within 96 h after i.v. injection ($n = 4$, bars represent means ± SD).

We next measured the tissue and intratumoral Dox concentrations in mice bearing HT-29 tumors after i.v. administration of HFn-Dox NPs and compared with the same dose of free Dox and nontargeted liposomal Dox (Doxil). At 1, 4, and 24 h postinjection the tumors and normal tissues were excised and the concentration of Dox was measured. As shown in Fig. 4*B*, the intratumoral Dox concentration of the HFn-Dox–treated group showed about a 10-fold and fivefold increase compared with that in the free Dox and Doxil-treated group, respectively, at all of the three time points. The dramatically enhanced tumor drug uptake of the HFn-Dox group is attributed both to the high blood AUC and to the TfR1-mediated active tumor targeting. Equally important, HFn-Dox significantly reduced Dox concentrations in healthy organs over free Dox and Doxil, including the muscle, lung, kidney, spleen, intestine (Fig. S3) and heart (Fig. 4*C*). In particular, the encapsulation of Dox into HFn nanocages resulted in a 3.0- to 16.8-fold decrease in the drug concentration in the heart compared with free Dox and Doxil at 1, 4, and 24 h postinjection. This resulted in a substantial decrease in Dox-associated cardiomyopathy in the HFn-Dox–treated group, as shown by the H&E staining of heart sections and the heart weight test (Fig. S4). The increase of tumor exposure and decrease of healthy organ exposure to Dox indicate higher achievable drug doses when the dose-limiting heart toxicity is controlled.

We further examined the total body clearance of HFn-Dox by measuring the Dox contents of excreted excrement and carcass retention. Ninety-six hours after i.v. injection of HFn-Dox into healthy mice over 70% of HFn-Dox was eliminated from the body via the kidney (into urine) and liver (into feces) (Fig. 4*D*), further confirming that HFn-Dox NPs can be efficiently cleared from the body, thus resulting in minimal exposure of healthy organs to Dox. The total body clearance experiment in HT-29 tumor-bearing mice showed that about 55% of the i.v. injected HFn-Dox was cleared from the whole body within 96 h postinjection

(Fig. S5). The difference in body clearance between the two groups again indicates the specific accumulation of HFn-Dox in tumors.

To assess the Dox-associated toxicity of HFn-Dox NPs, we performed a single-dose tolerability study. Healthy BALB/c mice were i.v. administered HFn-Dox or free Dox at increasing doses and monitored for body weight, blood chemistry, and clinical observations. The maximum tolerated doses (MTDs) for a single injection of free Dox and HFn-Dox were determined to be 5 mg/kg mouse body weight and 20 mg/kg body weight Dox equivalents, respectively (Fig. S6). No abnormal clinical observations or appreciable body weight loss were observed in mice treated with HFn-Dox at its MTD (Fig. S6). The corresponding blood chemistry parameters also exhibited no significant differences relative to the PBS-treated control mice (Table S1), verifying the safety of HFn-Dox treatment at its MTD. These results demonstrate that the encapsulation of Dox into HFn nanocages improves the drug's tolerability and thus increases the absolute concentration of Dox in the tumor.

We next evaluated the therapeutic effects of HFn-Dox at its MTD in HT-29 tumor models and compared it with the same dose of clinically approved Doxil. A single dose of HFn-Dox, Doxil, free Dox, empty HFn nanocage, or PBS was injected i.v. into mice after the tumors reached ~100 mm^3. Mice with tumor sizes of 100 mm^3 are generally used to investigate drug effects. This is because solid tumors typically display Gompertzian kinetics (35), and they are typically found to be in a log phase of growth when at a size of 100 mm^3, where the new tumor vessels are robustly developing and no necrosis in the interior of the tumor has appeared yet (36). The tumors in free Dox-, free HFn-, or PBS-treated groups grew rapidly, and the average volume of tumors reached >1,000 mm^3 on day 18 after tumor implantation (Fig. 5*A*). A single injection of Doxil (20 mg/kg Dox equivalents) reduced the tumor growth rate slightly. Importantly, treatment with HFn-Dox at its MTD (20 mg/kg Dox equivalents) resulted in clearly visible regression of tumor growth, which correlated well with a substantial increase in animal survival (Fig. 5*B*). The average survival times for mice treated with PBS, free Dox, or free HFn were 17, 18, and 18 d, respectively, whereas treatment with Doxil increased survival to 23 d. In contrast, treatment with HFn-Dox resulted in an 83.3% survival of mice for up to 40 d of the experiment. This was a significant improvement over free Dox (Kaplan–Meier, $P = 0.0004$) as well as Doxil (Kaplan–Meier, $P = 0007$). With regard to the toxicity as detected by the loss of body weight, HFn-Dox at MTD seemed to be well tolerated with a mean weight loss at nadir of 6.7% (Fig. 5*C*). Mice receiving Doxil at the same concentration exhibited high toxicity, and four of seven treated mice died within 23 d post-implantation, even though the mean body weight loss at nadir was less than 15%, indicating a significantly higher toxicity of Doxil than of HFn-Dox.

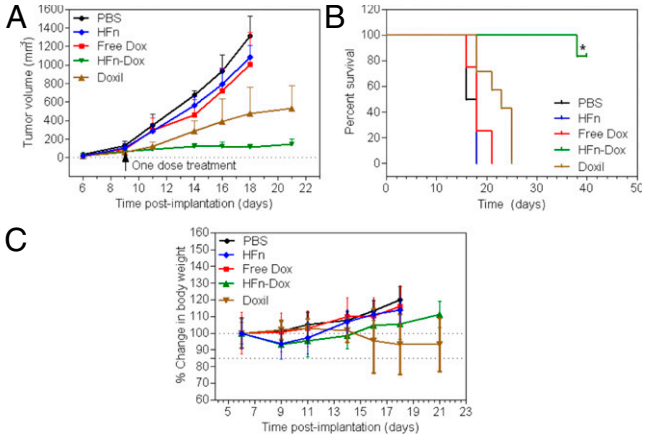

Fig. 5. Antitumor activity and toxicity of HFn-Dox NPs. HT-29 tumor cells were implanted s.c. into mice on day 0. Mice were treated with HFn-Dox (20 mg/kg Dox equivalents; $n = 6$), Doxil (20 mg/kg Dox equivalents; $n = 7$), free Dox (5 mg/kg; $n = 8$), HFn nanocages (480 mg/kg; $n = 8$), or PBS ($n = 6$) at day 9. (*A*) Tumor growth curves for mouse groups are indicated. (*B*) Animal survival curves in different groups. Asterisks indicate $P = 0.0004$ and 0.0007 for HFn-Dox compared with free Dox and Doxil, respectively (Kaplan–Meier). (*C*) The effect of different treatments on mouse body weight (bars represent means ± SD, $n = 4$–8).

The low in vivo toxicity of HFn-Dox NPs is not because human HFn does not interact with mouse cells, because we detected a cross-reaction between human HFn and murine cell surface receptors by flow cytometric analysis in mouse cells (Fig. S7).

To examine the universal antitumor effect of HFn-Dox NPs, A375 human melanoma and MDA-MB-231 human breast cancer xenograft models were also used (Fig. S8). At the administered dose of 20 mg/kg Dox equivalents, HFn-Dox and Doxil showed similar inhibition of tumor growth in both model systems. However, the mice treated with Doxil experienced severe drug toxicity, and the majority of treated mice died within 15 d postimplantation and displayed more than 15% body weight loss (without recovery) in both A375 and MDA-MB-231 models. The median survival time of Doxil-treated mice was 14 d in both A375 and MDA-MB-231 tumor models. In contrast, treatment with HFn-Dox resulted in 100% survival of the mice in both tumor models over the 40-d period of study. These results indicated that HFn-Dox possesses a substantial and universal antitumor activity with only a single-dose treatment.

Discussion

To date, only a handful of tumor-targeted nanocarriers and approaches have entered clinical trials, even though targeting of therapeutic drugs to diseased cells and tissues was first suggested more than 100 y ago (37). Importantly, so far none of these carriers has been approved for clinical use owing to the complexity of designing particles that can meet all of the design criteria of targeted drug delivery (38). Our newly developed natural HFn nanocarrier specifically delivers high doses of Dox to tumor cells without the requirement for additional ligand modification or property modulation. In comparison with conventional engineered NPs, the natural HFn nanocarrier system has several advantages, discussed below.

Intrinsic Tumor Targeting Ability. Without any ligand functionalization, HFn can specifically deliver Dox into tumor cells through TfR1-mediated targeting and the following receptor-mediated endocytosis. Artificial NPs, however, are typically modified with targeting ligands such as antibodies or peptides using complicated processes and expensive reagents to achieve tumor-specific targeting. These complicated modification processes often result in high cost, low purity, and variations in the final product, which make it difficult for these artificial systems to enter into clinical practice. In addition, the inappropriate density of targeting ligands on the surface of carrier particles might trigger immune responses against the carrier (39).

Favorable Pharmacokinetics and Safety Profiles. The in vivo characteristics of carrier particles are largely determined by their surface physicochemical properties. However, it is challenging to enable an artificial particle with optimal surface characteristics that simultaneously confer specific tumor targeting, favorable in vivo behavior, and excellent biocompatibility. So far, the application of any targeting NPs has not been approved by the US Food and Drug Administration, reflecting the difficulties of making NPs that can meet all of the criteria for specific drug delivery.

HFn exists naturally in the human body and does not contain any potentially toxic elements that would activate inflammatory or immunological responses and thus exhibits excellent biocompatibility when used in vivo. In addition, the size of HFn nanocages is 12 nm, which is ideal for anticancer nanomedicine because they can fully overcome the physiological barriers posed by the tumor microenvironment and actively make their way deep into the tumor tissues (40). Combined with their intrinsic tumor-targeting property, HFn-Dox NPs showed a long plasma half-life (256 ± 19.0 versus 21 ± 6.4 min for free Dox) and high AUC (1,192 ± 99.38 versus 5.7 ± 0.33%ID·mL^{-1}·min^{-1} for free Dox), high drug accumulation in tumors (10-fold higher than in free Dox-treated mice and fivefold higher than in Doxil-treated mice), and low drug exposure of normal organs and were efficiently cleared from the body. These properties of HFn nanocages largely improve the therapeutic efficiency of Dox while reducing its toxic side effects.

Excellent Antitumor Activity. In all three tumor models used here, HFn-Dox NPs displayed a significantly longer median survival time, as well as lower toxicity compared with the clinically approved Doxil, demonstrating a substantial antitumor activity of HFn-Dox. The improved antitumor effects of HFn-Dox over Doxil can be explained by the combined contribution of active tumor targeting, efficient endocytosis, and optimal physicochemical properties of HFn.

Easy Scaling-Up and Manufacturing with Robust and Reproducible Procedures. Another main challenge for clinical translation of engineered carrier particles is how to perform efficient scale-up of their production while maintaining all the characteristics that determine their therapeutic efficiency. Natural HFn nanocages are produced in *E. coli* at high yield and can be easily purified by exploiting their heat-resistant property (17, 26). In addition, HFn exhibits favorable in vivo pharmacokinetics, excellent biocompatibility, and tumor-targeting activity without the modification of any ligands or surface modulation of physicochemical properties. Thus, the well-defined, single-component particle system of natural HFn makes it easy to scale-up the manufacturing process with reproducible procedures that fulfill the need of clinical trials.

Universal Drug-Loading Platform. The loading of the foreign molecule Dox into HFn nanocages is dependent on their electrostatic interactions. Because the pK_a of doxorubicin is 8.2 (31), it can easily bind to the negatively charged internal surface of ferritin nanocages (32) in the neutral loading buffer. Therefore, it can be assumed that any small-molecule chemotherapeutic drugs that form positively charged groups in neutral aqueous solutions can be loaded into the cavity of an HFn nanocage. Such positively charged drugs include most of alkylating agents (41), cisplatin and some of its derivatives (41), a number of antibiotics (such as Dox, daunorubicin, and idarubicin) (42), and the plant alkaloid vinblastine (43), among others. In addition, it was reported that Cu-64 (12) and U-235 (24) radioisotopes can also be encapsulated into ferritin nanocages by association with the metal-binding sites at the surface of ferritin nanocages, just like the way iron ions do. Thus, we assume that the commonly used medical radioisotopes such as gallium-67, rubidium-82, copper-64, technetium-99m, indium-111, xenon-133, thallium-201, and yttrium-90 can also be loaded into HFn nanocages for tumor-targeted therapy and diagnosis. So far, a great number of foreign molecules have been successfully encapsulated into ferritin nanocages (18–24), indicating that HFn is a universal drug carrier for tumor-targeted delivery.

Materials and Methods

Detailed descriptions of the preparation and characterization of the HFn-Dox NPs, in vitro Dox release studies, antibody blocking assays, MTD, and biodistribution studies can be found in *SI Text*.

Labeling of HFn-Dox. HFn-Dox and HFn were labeled with the fluorescent dye Cy5.5 by the following procedures. The Cy5.5-NHS ester (GE Healthcare) was dissolved in dry DMSO (Sigma-Aldrich) and added to HFn-Dox or HFn solution (0.1 M $NaHCO_3$, pH 8.5), at a dye to HFn-Dox or HFn molar ratio of 10:1. The mixture was gently stirred overnight at 4 °C in the dark and then purified on a polyacrylamide column (molecular weight cut-off 6,000; Thermo Scientific) to remove free dyes. The concentration of labeled Cy5.5 was determined by measuring the absorbance at 673 nm and the concentration of HFn was determined using a Bradford assay kit (Bio-Rad).

Iodination of HFn-Dox was performed using the Iodogen method. Briefly, 0.72 mCi of ^{125}I (Beijing Atom High Tech) was mixed with 100 μg HFn-Dox in 100 μL PBS (0.2 M, pH 7.4) buffer and added into a vial coated with 50 μg Iodogen (Sigma-Aldrich). After incubation for 10 min at room temperature, the mixture was purified with a PD-10 column (Amersham). Labeling yield and radiochemical purity of the products were measured by instant thin-layer chromatography using 85% (vol/vol) methanol as eluant on a radio-thin layer scanner (Bioscan).

Cell Binding Assay. The human colon cancer cell line HT-29 was obtained from the American Type Culture Collection (catalog no. HTB-38) and was cultured in RPMI-1640 medium (Sigma-Aldrich) containing 10% (vol/vol) FCS (Sigma-Aldrich). Cells were tested for mycoplasma contamination before use. Flow cytometry was used to assess the binding activity of HFn-Dox and HFn to HT-29 tumor cells. Briefly, 100-μL cell suspensions (2.5×10^6 cells per milliliter) were incubated with 0.4 μM of Cy5.5-conjugated HFn or HFn-Dox for 45 min at 4 °C in PBS buffer containing 0.3% BSA. After three washes with cold PBS buffer, cells were analyzed immediately on a FACSCalibur flow cytometry system (Becton Dickinson).

A cell competition binding assay was performed to quantitatively assess the binding affinities of HFn and HFn-Dox. Cy5.5-conjugated HFn at 0.4 μM was incubated with HT-29 cells in the presence of increasing concentrations of unconjugated HFn or HFn-Dox from 0 to 100 μM. After three washes with cold PBS buffer, the binding of Cy5.5-HFn to HT-29 cells was analyzed by measuring the cell-associated fluorescence using flow cytometry. The best-fit IC_{50} values were calculated by fitting the data with nonlinear regression using GraphPad Prism 5.01 (GraphPad Software).

Cellular Uptake and Distribution. The cellular uptake and distribution of HFn-Dox were studied by confocal laser scanning microscopy. Briefly, HT-29 cells were seeded on poly-L-lysine–treated coverslips (BD Biosciences) and cultured in six-well plates (Corning) in RPMI-1640 medium with 10% (vol/vol) FCS overnight for cell attachment. Cells were then incubated with HFn-Dox (1 μM Dox equivalents) or Cy5.5-labeled HFn-Dox (1 μM Cy5.5 equivalents) at 37 °C for different times. After the incubation, the cells were washed with cold PBS, fixed in 4% (wt/vol) cold formaldehyde, and permeabilized with 0.1% Triton X-100. To visualize lysosomes, the cells were further incubated with an anti-Lamp1 mAb (1:200, clone H4A3; Invitrogen) at 37 °C for 1 h after blocking by 5% normal goat serum. The cells were then washed three times with PBS and incubated with goat anti-mouse IgG1 conjugated with Alexa-488 (1:500; Invitrogen) for 1 h at 37 °C. Nuclei were stained with DAPI (1 μg/mL; Roche Applied Science) for 10 min at room temperature. Images were collected by a confocal laser scanning microscope (Olympus). The fluorescent signal of Alexa-488 was collected from 500 to 550 nm to avoid interference of Dox-related fluorescence because they are both excited at 488 nm.

In Vivo Studies. All animal studies were performed with the approval of the Chinese Academy of Sciences Institutional Animal Care and Use Committee. For in vivo nuclear imaging, female BALB/c nude mice (Animal Center of the Chinese Academy of Medical Science) 6 wk old were s.c. implanted with 1×10^6 HT-29 tumor cells in the right upper flank. The cells were tested for mycoplasma contamination before implantation. When the size of tumors reached about 1.0 cm in diameter, mice were injected i.v. with 400 μCi of ^{125}I-labeled HFn-Dox in 100 μL saline and imaged at 1, 2, 4, and 24 h postinjection using an Infinia γ-camera (GE Healthcare).

For therapeutic assessment, female BALB/c nude mice bearing HT-29, A375, or MDA-MB-231 tumors of 100 mm^3 in size were randomly assigned to four or five groups (n = 5–10 mice in each group) and i.v. administered a single dose of HFn-Dox (20 mg/kg Dox equivalents), Doxil (20 mg/kg Dox equivalents), free Dox (5 mg/kg), free HFn cage (480 mg/kg, equivalent to

20 mg/kg Dox dose), or PBS. The volume of tumors and the body weight of the mice were measured three times a week during the experimental period. Tumor volume was determined by caliper measurements with the formula $V_{tumor} = L \times W^2/2$, where L and W refer to the maximum and minimum diameters, respectively. In each tumor model the mice were monitored for up to 40 d after implantation or until one of the following conditions for killing them was met: (*i*) 15% body weight loss or (*ii*) tumor greater than 1,000 mm^3. On day 40, all surviving mice were killed.

ACKNOWLEDGMENTS. We thank Xiaojun Huang and Gang Ji for excellent technical support in cryoelectron transmission microscopy imaging and gratefully acknowledge the support of the transmission EM facilities at the Center for Biological Imaging, Institute of Biophysics, Chinese Academy of Science. This work was supported in part by grants from the National Science and Technology Major Project (2012ZX10002009-016), Strategic Priority Research Program of the Chinese Academy of Sciences (XDA09030306), National Natural Science Foundation of China (81201698), and 973 Program (2011CB933503, 2015CB553705).

1. Salvador-Morales C, Valencia PM, Thakkar AB, Swanson EW, Langer R (2012) Recent developments in multifunctional hybrid nanoparticles: Opportunities and challenges in cancer therapy. *Front Biosci (Elite Ed)* 4:529–545.
2. Chauhan VP, Jain RK (2013) Strategies for advancing cancer nanomedicine. *Nat Mater* 12(11):958–962.
3. Gu F, et al. (2008) Precise engineering of targeted nanoparticles by using self-assembled biointegrated block copolymers. *Proc Natl Acad Sci USA* 105(7):2586–2591.
4. Choi CH, Zuckerman JE, Webster P, Davis ME (2011) Targeting kidney mesangium by nanoparticles of defined size. *Proc Natl Acad Sci USA* 108(16):6656–6661.
5. Ferrari M (2005) Cancer nanotechnology: Opportunities and challenges. *Nat Rev Cancer* 5(3):161–171.
6. Jain RK, Stylianopoulos T (2010) Delivering nanomedicine to solid tumors. *Nat Rev Clin Oncol* 7(11):653–664.
7. Theil EC (1987) Ferritin: Structure, gene regulation, and cellular function in animals, plants, and microorganisms. *Annu Rev Biochem* 56:289–315.
8. Meldrum FC, Heywood BR, Mann S (1992) Magnetoferritin: In vitro synthesis of a novel magnetic protein. *Science* 257(5069):522–523.
9. Wong KKW, Mann S (1996) Biomimetic synthesis of cadmium sulfide-ferritin nanocomposites. *Adv Mater* 8(11):928–932.
10. Klem MT, Mosolf J, Young M, Douglas T (2008) Photochemical mineralization of europium, titanium, and iron oxyhydroxide nanoparticles in the ferritin protein cage. *Inorg Chem* 47(7):2237–2239.
11. Li L, et al. (2010) Binding and uptake of H-ferritin are mediated by human transferrin receptor-1. *Proc Natl Acad Sci USA* 107(8):3505–3510.
12. Lin X, et al. (2011) Chimeric ferritin nanocages for multiple function loading and multimodal imaging. *Nano Lett* 11(2):814–819.
13. Zhen Z, et al. (2013) RGD-modified apoferritin nanoparticles for efficient drug delivery to tumors. *ACS Nano* 7(6):4830–4837.
14. Zhen Z, et al. (2013) Ferritin nanocages to encapsulate and deliver photosensitizers for efficient photodynamic therapy against cancer. *ACS Nano* 7(8):6988–6996.
15. Falvo E, et al. (2013) Antibody-drug conjugates: Targeting melanoma with cisplatin encapsulated in protein-cage nanoparticles based on human ferritin. *Nanoscale* 5(24): 12278–12285.
16. Li K, et al. (2012) Multifunctional ferritin cage nanostructures for fluorescence and MR imaging of tumor cells. *Nanoscale* 4(1):188–193.
17. Fan K, et al. (2012) Magnetoferritin nanoparticles for targeting and visualizing tumour tissues. *Nat Nanotechnol* 7(7):459–464.
18. Yang Z, et al. (2007) Encapsulation of platinum anticancer drugs by apoferritin. *Chem Commun (Camb)* 7(33):3453–3455.
19. Xing R, et al. (2009) Characterization and cellular uptake of platinum anticancer drugs encapsulated in apoferritin. *J Inorg Biochem* 103(7):1039–1044.
20. Yan F, Zhang Y, Kim KS, Yuan HK, Vo-Dinh T (2010) Cellular uptake and photodynamic activity of protein nanocages containing methylene blue photosensitizing drug. *Photochem Photobiol* 86(3):662–666.
21. Domínguez-Vera JM (2004) Iron(III) complexation of Desferrioxamine B encapsulated in apoferritin. *J Inorg Biochem* 98(3):469–472.
22. Cutrin JC, Crich SG, Burghelea D, Dastrù W, Aime S (2013) Curcumin/Gd loaded apoferritin: A novel "theranostic" agent to prevent hepatocellular damage in toxic induced acute hepatitis. *Mol Pharm* 10(5):2079–2085.
23. Butts CA, et al. (2009) Identification of a fluorescent general anesthetic, 1-aminoanthracene. *Proc Natl Acad Sci USA* 106(16):6501–6506.
24. Hainfeld JF (1992) Uranium-loaded apoferritin with antibodies attached: Molecular design for uranium neutron-capture therapy. *Proc Natl Acad Sci USA* 89(22):11064–11068.
25. Romagnani S (2006) Immunological tolerance and autoimmunity. *Intern Emerg Med* 1(3):187–196.
26. Uchida M, et al. (2006) Targeting of cancer cells with ferrimagnetic ferritin cage nanoparticles. *J Am Chem Soc* 128(51):16626–16633.
27. Jeon JO, et al. (2013) Designed nanocage displaying ligand-specific peptide bunches for high affinity and biological activity. *ACS Nano* 7(9):7462–7471.
28. Li X, et al. (2012) Epidermal growth factor-ferritin H-chain protein nanoparticles for tumor active targeting. *Small* 8(16):2505–2514.
29. Dehal PK, et al. (2010) Magnetizable antibody-like proteins. *Biotechnol J* 5(6): 596–604.
30. Kim M, et al. (2011) pH-dependent structures of ferritin and apoferritin in solution: Disassembly and reassembly. *Biomacromolecules* 12(5):1629–1640.
31. Yang SC, Ge HX, Hu Y, Jiang XQ, Yang CZ (2000) Doxorubicin-loaded poly (butylcyanoacrylate) nanoparticles produced by emulsifier-free emulsion polymerization. *J Appl Polym Sci* 78(3):517–526.
32. Harrison PM, Arosio P (1996) The ferritins: Molecular properties, iron storage function and cellular regulation. *Biochim Biophys Acta* 1275(3):161–203.
33. Arosio P, Ingrassia R, Cavadini P (2009) Ferritins: A family of molecules for iron storage, antioxidation and more. *Biochim Biophys Acta* 1790(7):589–599.
34. Tan H, et al. (2014) Visual and semi-quantitative analyses of dual-phase breast-specific gamma imaging with Tc-99m-sestamibi in detecting primary breast cancer. *Ann Nucl Med* 28(1):17–24.
35. Norton L, Simon R, Brereton HD, Bogden AE (1976) Predicting the course of Gompertzian growth. *Nature* 264(5586):542–545.
36. Frangioni JV (2008) New technologies for human cancer imaging. *J Clin Oncol* 26(24): 4012–4021.
37. Strebhardt K, Ullrich A (2008) Paul Ehrlich's magic bullet concept: 100 years of progress. *Nat Rev Cancer* 8(6):473–480.
38. Shi J, Xiao Z, Kamaly N, Farokhzad OC (2011) Self-assembled targeted nanoparticles: Evolution of technologies and bench to bedside translation. *Acc Chem Res* 44(10): 1123–1134.
39. Taneichi M, et al. (2006) Antigen chemically coupled to the surface of liposomes are cross-presented to CD8+ T cells and induce potent antitumor immunity. *J Immunol* 177(4):2324–2330.
40. Chauhan VP, et al. (2012) Normalization of tumour blood vessels improves the delivery of nanomedicines in a size-dependent manner. *Nat Nanotechnol* 7(6):383–388.
41. Siddik ZH (2002) Mechanisms of action of cancer chemotherapeutic agents: DNA-interactive alkylating agents and antitumour platinum-based drugs. *The Cancer Handbook*, ed Alison MR (Nature Publishing Group, London), pp 1125–1313.
42. Lown JW (1993) Discovery and development of anthracycline antitumor antibiotics. *Chem Soc Rev* 22(3):165–176.
43. Bau R, Jin KK (2000) Crystal structure of vinblastine. *J Chem Soc Perk T* 1(13):2079–2082.